Numerical simulation of fast granular flow facing obstacles on steep terrains

Su Yang, Xiaoliang Wang [*], Qingquan Liu, Menghan Pan

Department of Mechanics, School of Aerospace Engineering, Beijing Institute of Technology, Beijing 100081, China

ABSTRACT

The interaction between fast shallow granular flow and obstacles on steep terrain is an important aspect of granular mechanics and defending against geological hazards. In this study, we used a depth-averaged model for granular flow facing obstacles on steep terrains in a bed-fitted coordinate system where the obstacle system is treated as a local bed deviation term. A second-order Riemann-free scheme is extended to compute the depth-averaged model with a wetting–drying technique, which is verified by several granular flow cases, such as aluminum bar collapse and granular flow runout on a steep slope. Numerical simulations were performed for the case of granular flow facing a (i) single hemispherical obstacle and (ii) system of three hemispherical obstacles to produce a dynamical process and deposit profile, and show good agreement with experimental results. Granular flow facing a single obstacle on a concave plane produces a detached shock wave that moves upstream and a tailing rapid transition zone that moves down, which will merge to form a new shock for deposition. Granular flows facing a three-hemisphere obstacle system produce a tailing rapid transition zone that moves downstream and a downstream wavy shock that results from the interaction of three bow shocks in front of each obstacle. The downstream wavy shock moves upstream and merges with the upstream transition zone to form a new curved shock, which later relaxes to a deposit owing to bed friction. These findings provide some supplemental understandings of flow structures of fast granular flow facing obstacles.

© 2020 Elsevier Ltd. All rights reserved.

1. Introduction

Large-scale granular material-dominated hazards can cause great loss to human life and infrastructure (Intrieri et al., 2018; Tang et al., 2011; Pudasaini and Mergili, 2019; Mergili et al., 2020a,b). The interaction between granular material-dominated flow and structures (e.g., buildings) is particularly important in mountainous regions. The flow behavior past a structure and impact force are two fundamental problems involved in the interaction between granular flow and structures (Pudasaini and Hutter, 2007). The constitutive behavior and structure-interaction mode of granular material differs substantially from water flow-dominated hazards (e.g., floods). Granular material exhibits both solid and fluid behavior during motion (Domnik and Pudasaini, 2012; Domnik et al., 2013) and its interaction with structures involves both bypasses and impacts; processes which have gathered substantial research and engineering attention (Faug, 2015; Kattel et al., 2018).

---

* Corresponding author.
  E-mail address: wangxiaoliang52086@126.com (X. Wang).

Many experimental and numerical achievements have been reported in this field in recent years. Tang and Hu (2018) carried out 25 experiments of granular material-impacting obstacles and showed that the ratio of maximum impact time and structural vibration period change linearly with the Froude number. In an experimental study, Armanini et al. (2020) investigated the impact of a granular–liquid mixture on the wall of a channel, an interaction process that includes a reflected wave and vertical jet, and provided a simplified expression for the impact force. Wang et al. (2018) studied the impact process of debris flow on piers through large-scale indoor experiments and showed that layering effects exist in highly viscous debris flow but not in low-viscosity debris flow. Choi et al. (2014) carried out flume experiments on the impact of granular flow on baffle and studied the influence of baffle height, arrangement, and spacing on the flow process and energy dissipation. Caviedes-Voullième et al. (2014) carried out a systematic experimental study on granular flow facing obstacles on steep terrain and used advanced sensors to record the evolution of depth and complex wave structures during the interaction between granular flow and different obstacles. Pudasaini et al. (2007) performed laboratory experiments of dry granular chute flows impinging an obstructing wall. This leads to a sudden change in the flow regime from a fast moving supercritical thin layer to a stagnant thick heap with variable thickness and a surface dictated by the angle of repose typical for the material. They conducted particle image velocimetry (PIV) measurements. Analysis of the shock front formation and propagation upslope, evolution of the height of the supercritical flow, impact velocity and momentum are presented and discussed in detail. Similarly, Pudasaini and Kroener (2008) numerically studied strong shocks in rapid dense granular flows and compare with experimental data by Pudasaini et al. (2007). The rapidly moving material down the chute impinges on an obstruction wall erected perpendicular at the end of a long and steep channel. Impact leads to a sudden change in the flow regime. They present results about the depth and the velocity evolution and their comparisons with theoretical predictions associated with frictional granular flow equations incorporating anisotropic pressure conditions. The dynamical and geometrical effects of the flow were discussed in detail. These include geometry evolution and depositions at supercritical and subcritical flows, the impact velocity, shock speed, its position and evolution, choice of numerical limiters, and the influence of friction angles on the dynamics and depositions. An excellent agreement between theoretical predictions and experimental observations were demonstrated.

Teufelsbauer et al. (2011) developed a discrete element model (DEM) for dry particle flow on an inclined plane, reported that a DEM with constraint rotation more accurately reflects dry granular material, and also simulated runout, deposition, and impact processes. Calvetti et al. (2017) established a DEM model for dry particle flow past obstacles and studied the influence of initial volume, velocity distribution, height, and porosity of the granular deposit on the interaction force, which led to the development of an empirical formula. Zhou et al. (2020) studied the climbing height of a debris flow impacting a slit dam by DEM and provided an analytical expression through the momentum theorem. Bi et al. (2018) studied the influence of an obstacle array of different row and column spacing on the impact force of granular flow on structures using DEM simulations. Dai et al. (2016) established a smoothed particle hydrodynamics (SPH) model for debris flows over a check dam, in which the former was modeled as a viscous fluid and the latter as an elastic solid, which was used to study the impact force evolution process of debris flows impacting check dams in Wenjiagou and Hongchungou, China. Kattel et al. (2018) performed simulations on two-phase mass flows (Pudasaini, 2012) with a high-resolution and efficient numerical scheme that is capable of capturing rapid and detailed dynamics, including the strongly re-directed flow with multiple stream lines, mass arrest, strong shock waves and debris-vacuum generation and flow pattern formations, as the rapidly cascading mass suddenly encounters the obstacles. The estimated impact pressure is useful for designing the defense structures. The solid and fluid phases show fundamentally different interactions with obstacles, flow spreading and dispersions, and run-out dynamics and deposition. The observations are in line with natural debris flows and experiments. Gray et al. (2003) simulated shock waves, dead zones, and particle-free rapid granular flows past a tetrahedron using a depth-integrated model and taking the obstacle as a source term. Cui and Gray (2013) investigated granular flows facing a cylinder treated as a boundary. Juez et al. (2014) established a shallow water-like model with a modified gravity term representing steep terrain effects to simulate granular flow past a single hemisphere and three hemispheres. The results agreed qualitatively well with their experiments with some deviations around the obstacles.

From the above survey, we found that the interaction between granular flow and obstacles has achieved several progresses in structure formation via either numerical or experimental method. However, the interaction problem includes both bypass and run-ups, as well as shock formation, interaction and deposition in granular flow facing obstacles. The experiments borrow from several classical methods used in hydraulics, which may not be able to reflect meso-scale structures of granular flow in detail, such as shock formation and interaction, and excludes several mechanisms and physics owing to the limited selection of physical parameters for granular material and obstacle structures. The DEM model addresses difficulties in contacting law, parameter calibration, and time consumption due to real particle scaling effects. Meshless methods such as SPH require sophisticated constitutive models, which are not yet well developed for granular material, and the artificial boundary treatment technique is likely questionable in granular flow simulations. There are strong couplings between granular flow and obstacles (e.g., bypass, run-up, steep terrain effects), which lead to a complex flow behavior, especially for shock formation and interaction of granular flow past obstacles (Pudasaini and Hutter, 2007; Faug, 2015; Kattel et al., 2018; Kafle et al., 2019). However, both the impact forces and flow behavior of granular flow facing obstacles still remain poorly understood.

In this study, we address the flow behavior of a fast granular flow facing obstacles. The objective is to develop an efficient numerical model to simulate both bypass, run-up, and shock waves in the granular flow facing obstacles on steep terrains, and in particular, to extract shock formation and interaction physics of the granular flow.

The remainder of this paper is arranged as follows. The mathematical equations and numerical schemes are presented in Section 2. Two cases of different kinds of granular flow are simulated to verify the numerical model in Section 3. The interaction between granular flow and obstacles including a hemisphere and three hemispheres is studied with discussions on shock wave formation and interaction in Section 4, followed by conclusions and perspectives.

2. Governing equations and numerical methods

2.1. Governing equations

We formulate the governing equations in a depth-integrated framework in a local bed-fitted coordinate system for granular flow past obstacles on steep terrains, as shown in Fig. 1. The conservative form of the governing equation is given as (Gray et al., 1999; Pudasaini and Hutter, 2003).

$$\frac{\partial \mathbf{U}}{\partial t} + \frac{\partial \mathbf{F}}{\partial x} + \frac{\partial \mathbf{G}}{\partial y} = \mathbf{s}, \tag{1}$$

where t represents time, x and y are downslope and cross-slope coordinates, and vectors $\mathbf{U}$, $\mathbf{F}$, $\mathbf{G}$ and $\mathbf{s}$ denote the conserved flow variables, fluxes in two directions, and source terms, respectively:

$$\mathbf{U} = \begin{pmatrix} h \\ hu \\ hv \end{pmatrix}, \mathbf{F} = \begin{pmatrix} hu \\ hu^2 + \frac{1}{2}k_x g_z h^2 \\ huv \end{pmatrix}, \mathbf{G} = \begin{pmatrix} hv \\ huv \\ hv^2 + \frac{1}{2}k_y g_z h^2 \end{pmatrix},$$

$$\mathbf{s} = h \begin{pmatrix} 0 \\ g_x - \frac{u}{\sqrt{u^2+v^2}} \tan\delta(g_z + \frac{u^2}{r_x}) - g_z \frac{\partial z_b}{\partial x} \\ g_y - \frac{v}{\sqrt{u^2+v^2}} \tan\delta(g_z + \frac{v^2}{r_y}) - g_z \frac{\partial z_b}{\partial y} \end{pmatrix}, \tag{2}$$

Here, h is depth, u and v are depth-averaged velocities in x and y directions, $(g_x \quad g_y \quad g_z)^T$ is the gravity vector, r_x and r_y are curvature radii, and z_b is the local bed variation deviating from the main curved bed surface (Wang et al., 2004; Pudasaini and Hutter, 2007).

Granular material is considerably different from water, which exhibits both solid and flow behavior. A constitutive relationship should therefore be appropriately chosen. We choose Coulomb friction model for bed resistance, and the earth pressure theory from soil mechanics to account stress anisotropy (Savage and Hutter, 1989; Pudasaini and Hutter, 2007). As shown in the source term, k_x and k_y are earth pressure coefficients, where $k_x = 2\left(1 \mp \sqrt{1 - \cos^2\phi \sec^2\delta}\right)\sec^2\phi - 1$ and $k_y = \frac{1}{2}\left(1 + k_x \mp \sqrt{(1-k_x)^2 + 4\tan^2\delta}\right)$, in which respectively, the active ('−') sign is for extension (positive velocity gradient) and the passive ('+') earth pressure coefficient is chosen for contraction (negative velocity gradient). ϕ and δ are the internal and bed friction angles (Wang et al., 2004; Pudasaini and Hutter, 2007).

2.2. Treatment of obstacle and terrain

Simulations of granular flow on steep terrain with obstacles meets difficulties in both the accuracy of flow modeling and the handling of obstacles. In this study, a bed-fitted coordinate system is selected for granular flow and the obstacle is regarded as a deviation from the main bed. For more detail on this, we refer to Pudasaini and Hutter (2003, 2007), and Kattel et al. (2018). As shown in Fig. 1, the main curved surface is chosen to generate a bed-fitted coordinate system, where the governing equation is formulated for the granular material (purple bump in Fig. 1). The deviation from the bed is represented by a local bed variation field function that includes the obstacles (brown lines in Fig. 1).

There are two scenarios in our numerical code to specify the terrain and obstacles. The first one is a parameter-based scenario composed of a straight inclined plane upstream and a horizontal runout zone downstream linked with a transition zone of arc type as shown in Fig. 1. This scheme is similar to Wang et al. (2004), without considering the channel twist effect (Pudasaini and Hutter, 2007). Parameters combination (θ, x_l, x_r) are provided by users to generated the slope scenario, as shown in Fig. 1, where θ denotes the upstream plane inclination, x_l and x_r are start and end of transition zone. While for obstacles, we have provided a parameterized method to generate four kinds of obstacles including hemi-ellipsoid, cuboid, cylinder, and tetrahedral, which could produce several kinds of obstacle systems with combinations. In the second scenario, users need to supply table of slope, curvature, obstacle height etc. All of the following computation are performed by the first scenario.
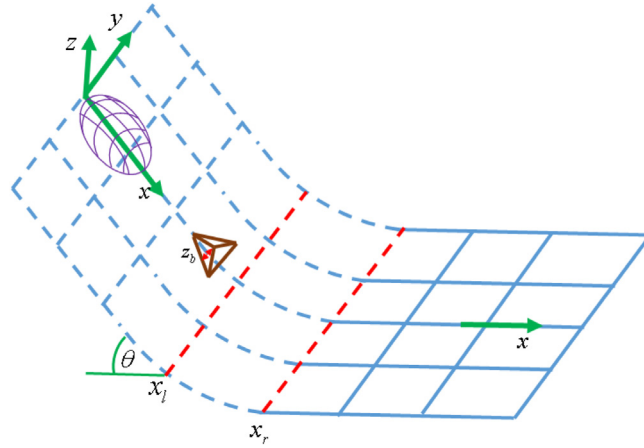
Fig. 1. Illustration of granular flow past obstacles on steep curved terrain. The brown bump represents obstacles and the purple curve is granular material. (x, y, z) is bed-fitted coordinates. Plane of inclination angle θ is to the left of red dashed line x_l, region in between the two dashed lines (x_l, x_r) is transition area, and runout zone is to the right of the red dashed line x_r.. (For interpretation of the references to color in this figure legend, the reader is referred to the web version of this article.)
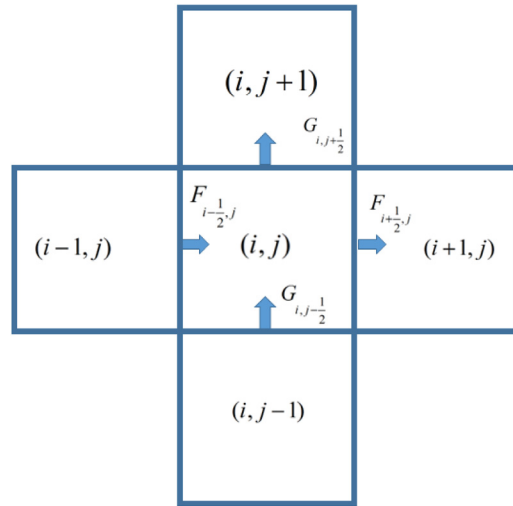
Fig. 2. Indexes for the mesh and numerical fluxes. All physical variables are defined in cells denoting by pairs (i, j), and fluxes such as $F_{i+\frac{1}{2},j}$ and $G_{i,j+\frac{1}{2}}$ are defined on the cell boundaries.

2.3. Numerical methods

The governing equation in Eq. (1) is a hyperbolic system with source terms (Pudasaini and Hutter, 2007). The hyperbolic structure on the left side may produce shocks and the source term accounts for the dissipation and deposition processes (Gray et al., 2003; Pudasaini and Hutter, 2007; Pudasaini, 2014; Kattel et al., 2018). The numerical scheme should therefore be able to capture shocks, predict the wetting–drying interface, and handle the stop–start behavior. We extended the Riemann-free scheme recently developed by Kurganov and Petrova (2007) for shallow water model to compute the conservation equation in Eq. (1) on a mesh (Fig. 2) via finite volume methods.

The cell-averaged value is defined as $U_{i,j} = \frac{1}{\Delta x \Delta y} \int U dx dy$, then for the cell (i, j), the update scheme of the left part of Eq. (1) is:

$$U_{i,j}^{(k+1)} = U_{i,j}^k - \frac{\Delta t}{\Delta x} \left(F_{i+\frac{1}{2},j} - F_{i-\frac{1}{2},j} \right) - \frac{\Delta t}{\Delta y} \left(G_{i,j+\frac{1}{2}} - G_{i,j-\frac{1}{2}} \right) \tag{3}$$

where $F_{i+\frac{1}{2},j}$ and $G_{i,j+\frac{1}{2}}$ are numerical fluxes on the right and top surface of cell (i, j), Δt is the time step, Δx and Δy are cell sizes

The numerical fluxes $F_{i+\frac{1}{2},j}$ are computed using a Riemann-free solver developed by Kurganov and Petrova (2007):

$$F_{i+\frac{1}{2},j} = \frac{a^+_{i+\frac{1}{2},j}F(U^-_{i+\frac{1}{2},j}) - a^-_{i+\frac{1}{2},j}F(U^+_{i+\frac{1}{2},j})}{a^+_{i+\frac{1}{2},j} - a^-_{i+\frac{1}{2},j}} + \frac{a^+_{i+\frac{1}{2},j}a^-_{i+\frac{1}{2},j}}{a^+_{i+\frac{1}{2},j} - a^-_{i+\frac{1}{2},j}}\left(U^+_{i+\frac{1}{2},j} - U^-_{i+\frac{1}{2},j}\right) \tag{4}$$

Where $U^+_{i+\frac{1}{2},j}$ and $U^-_{i+\frac{1}{2},j}$ are extrapolated vectors on the right-hand side of cell (i,j) using a monotonic upstream scheme for conservation laws (MUSCL) to suppress spurious oscillations, $a^+_{i+\frac{1}{2},j}$ and $a^-_{i+\frac{1}{2},j}$ are the largest and smallest extrapolated wave speeds (eigenvalues of the Jacobian $\frac{\partial F}{\partial U}$) at both sides of cell (i,j), respectively (Kurganov and Petrova, 2007; LeVeque, 2002). The computation procedure of flux $G_{i,j+\frac{1}{2}}$ follows the same technique of $F_{i+\frac{1}{2},j}$.

In order to handle the moving boundary/front of granular flow in a unified computation framework, we use a modified wetting–drying technique from our former study (Wang and Li, 2017). A dry cell is defined where the depth in a cell is less than a small value ε. If the depth of both sides of a face is smaller than ε, then the fluxes are zero. For those cells with depth smaller than ε, only mass conservation is computed while the momentum and velocity are set as zero. In this way, we can avoid nonphysical results, such as negative depth. In this study, ε is 10^{-6}.

A Strang splitting method computes the friction term with a stop–start technique (LeVeque, 2002). Similar to that used in shallow water flow (Liang and Marche, 2009), the velocity in a cell is set as zero if the flow turns back in that cell for a large friction force during one time step.

3. Model verification

We simulated two examples of granular flow to verify the abilities of wetting–drying front capturing and rapid granular flow dynamics on steep terrain. Simulations of interaction of rapid granular flow and obstacles will be presented in Section 4. Examples in this section includes the aluminum bar deposit collapse problem, and runout of granular flow along a slope.

3.1. Aluminum bar collapse

The column collapse of aluminum bars is a typical large deformation experiment involving granular material, for which Bui et al. (2008) observed the profile evolution, large deformation process, and localized failure zone. Using the numerical model, we simulated the collapse of aluminum bars. As shown in Fig. 3, the computation region was 0.6×0.2 m. Initially, a box of granular material with a height of 0.1 m was placed in the region $[0, 0.2 \text{ m}] \times [0, 0.2 \text{ m}]$ with a dry bed to the right. The internal friction angle $\phi = 19.8°$ and bed friction angle $\delta = 19.8°$ are used according to Bui's experimental measure. The mesh in this case was 400×400.

Fig. 3 shows the final profile of the numerical results along a typical slice surface ($y = 0.1$ m), which nearly coincides with the experimental counterpart with some deviation on the upper side. Although the above model and its numerical schemes are derived and applied for fast granular avalanches, they can still well simulate large deformation problems if only considering the information of height evolution. Computational consumption is relatively cheaper than that of a large deformation method (e.g., SPH) (An et al., 2016), but the internal deformation and failure information can only be obtained using the large deformation method for the full equation, as in Domnik and Pudasaini (2012) and Domnik et al. (2013).

3.2. Runout of a granular deposit on a slope

There is no analytical solution for two-dimensional granular flow. We therefore simulated the runout flow of a granular deposit on a slope, which has been experimentally studied by Koch et al. (1994). The experiment was implemented on a curved plane (3 m long, 2 m wide) with a cylindrical transition zone from 1.75 to 2.15 m, as shown by red dashed lines in Fig. 4. To the left of the transition zone, a plane with a slope of 45° and a horizontal plate are to the right for runout. A hemispherical cap with a radius of 18.5 cm filled with granular material on the sloped plane is quickly released to run down the curved slope.

We simulated experiment no. 2 where quartz materials flow down to the runout zone using a mesh of 400×400. The physical parameters follow the experimental results of Koch et al. (1994) where $\phi = 39°$ and $\delta = 29°$. The numerical solutions are shown in Fig. 4. After release, the granular flow accelerates down the slope and also spreads in the width direction. While in the transition zone, the granular flow slows and flow front begins to deposit after runout in the transition zone. The fast tailing granular flow impacts on a slow or even static deposit forms a trailing curved shock wave, which is similar to the detached shock in supersonic flow past a blunt wing (Anderson, 1990). Fig. 4 also shows the outer boundary of the experimental results, where the circles represent cells filled with at least one layer of particles, and triangles denote cells with half of the region filled by particles. The numerical results agree well with the inner boundary of circles rather than the outer boundary of triangles. It is reasonable to assume that cells with fewer particles in the collision regime might be beyond the validity of the continuum theory.
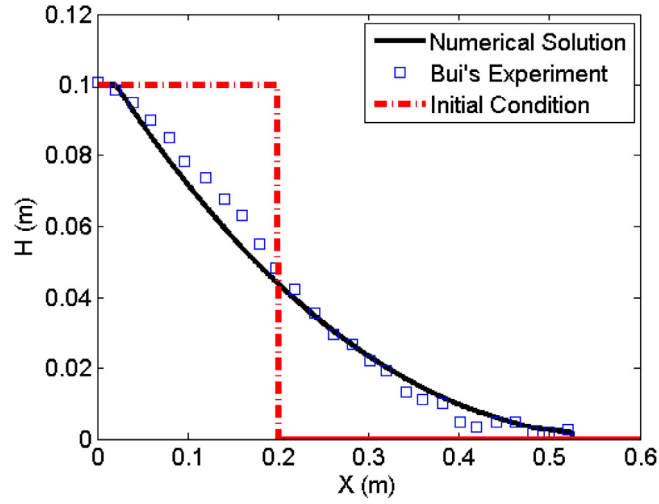
Fig. 3. Initial and final profiles of the collapse problem of aluminum bars: numerical vs experimental results.
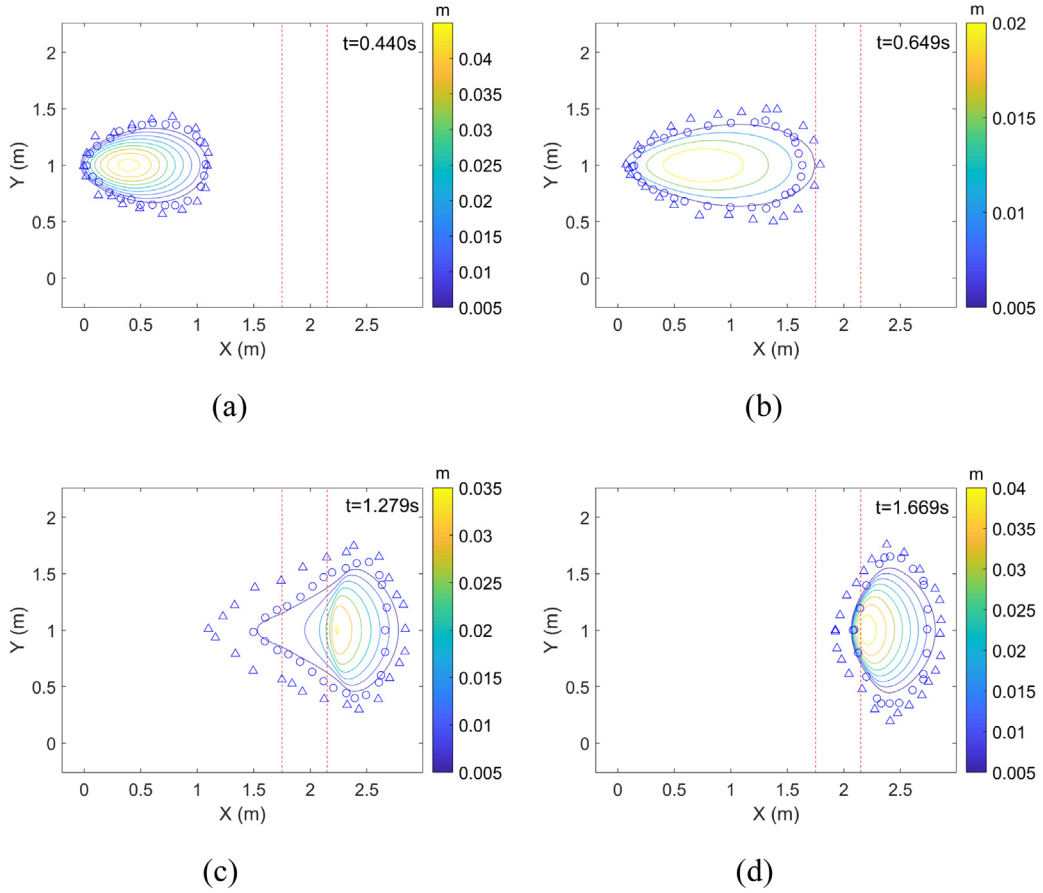

Fig. 4. Depth evolution of runout flow of granular flow along a slope: numerical and experimental comparison at different times. Area in between dashed lines is transition region, to the left is inclined plane, and to the right is runout zone.
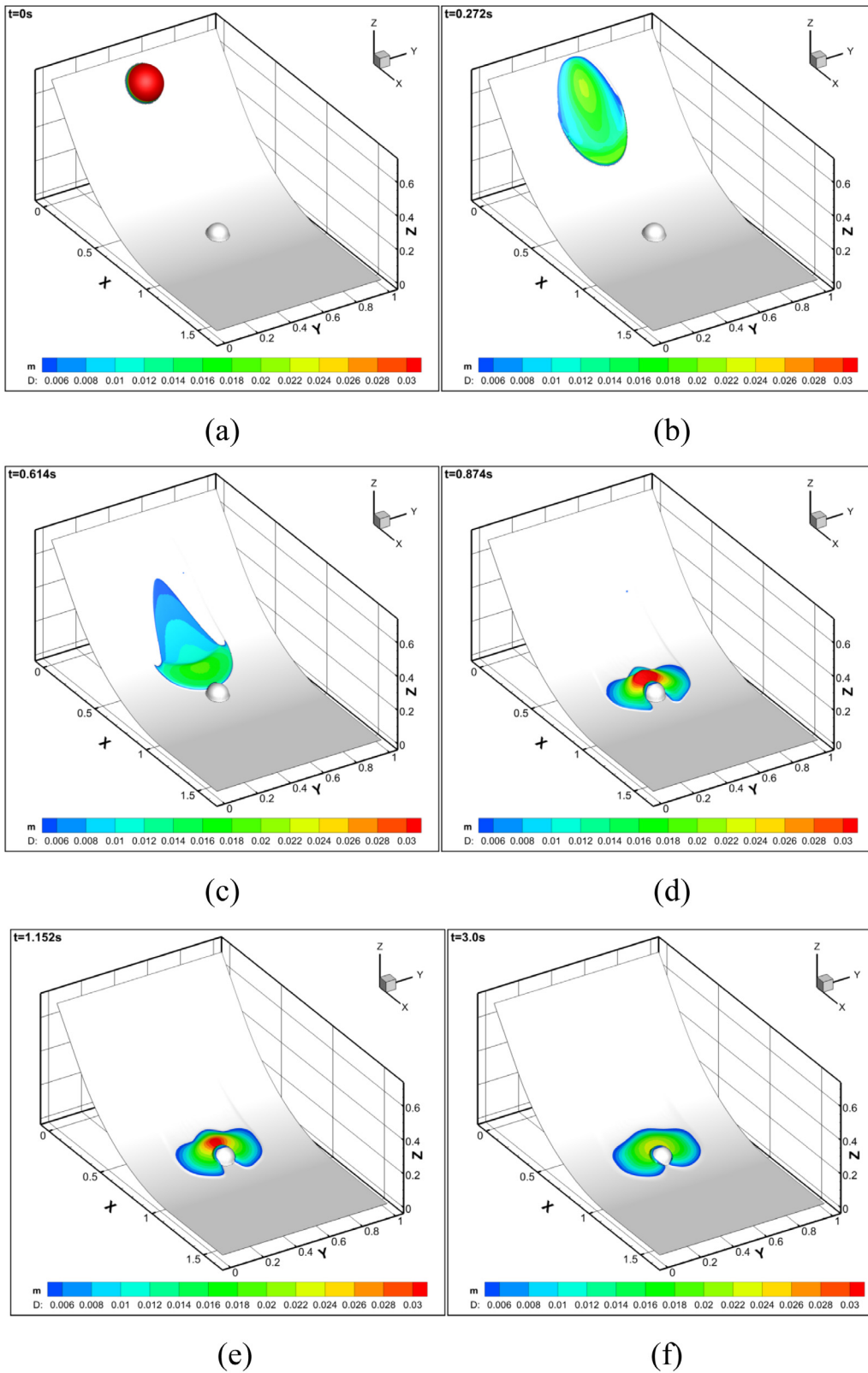
Fig. 5. Depth distribution evolution of granular flow past a hemispherical obstacle at different times.
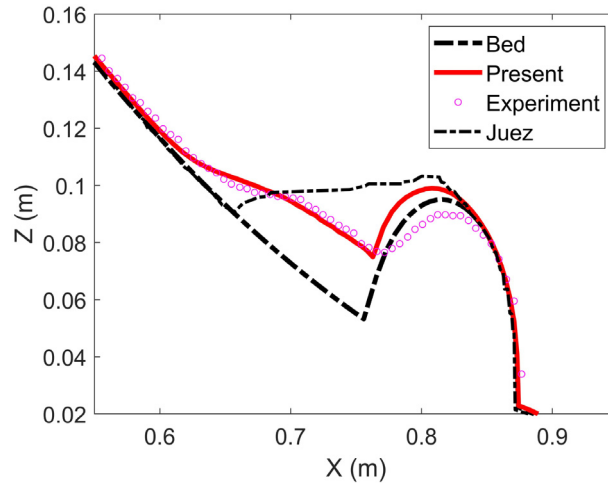
Fig. 6. Numerical simulations compared with Juez's experimental and computational results along the center slice for granular flow past a hemispherical obstacle.

4. Results and discussions

Obstacle is usually used to block granular flow or change the flow direction to mitigate granular-flow dominated hazard (Johannesson et al., 2009; Kattel et al., 2018). In this section we presented numerical simulation to assess the interaction of granular flow against an obstacle of hemisphere in 4.1 and an obstacle system composed of three hemi-spheres in 4.2.

4.1. Granular flow facing a single hemisphere

4.1.1. Simulation setup

We simulated granular flow facing a simple structure composed of a single hemisphere which was implemented by Caviedes-Voullième et al. (2014) through a careful experiment using sand and with all data recorded in a global coordinate system. We established a model of the first scenario with parameters combination (θ, x_l, x_r) of $(52°, 0.3573, 1.3680)$ with a horizontal runout plane instead since it does not affect the upstream flow, where the parameters are obtained through try and error. The computation domain was 1.88×1.0 m, which was discretized into a 400×400 mesh with a cell size of 4.7×2.5 mm. The internal friction angle is taken directly from the experiment results where $\phi = 34°$. We tested several values of the bed friction angle and found that a value of $34°$ is suitable for both the deposit and lateral extension. Through interpolation we find the positions of obstacles and initial bumps in the bed-fitted coordinate system. The hemispherical obstacle of 59 mm in radius was located at $(1.0834, 0.5)$ m. The initial granular bump with a 104-mm radius was located at $(0.1624, 0.5)$ m.

4.1.2. Granular flow process and deposition

Figs. 5a–5f show the numerical simulation results for granular flow past a single hemispherical obstacle. After release, the granular material accelerates downstream the slope and extends in the spanwise direction, as shown in Fig. 5b. When contacting the obstacle, the granular flow decelerates and tries to both run-up and bypass the obstacle to find a more easily accessible path (Fig. 5c). During this stage, a complex curved shock forms ahead of the obstacle and a fast tailing flows into a slower front in Fig. 5d. Owing to bed curvature, frictional resistance and the obstacle in the runout zone, the granular flow then slows quickly in Fig. 5e and relaxes to a stop in Fig. 5d. Interestingly, the detached shock structure seems to be frozen owing to the rapid slowdown in the runout zone.

Fig. 6 depicts the final deposition along the center slice where $y = 0.5$ m. The run-up and tailing distribution agree well with the experiment results, a bit better than Juez's model (Juez et al., 2014). As proved by Pudasaini and Kroener (2008), the earth pressure coefficient is an important mechanism of complex dynamics and deposits of granular material in rapid flowing stages against a rigid wall. In addition, the bed-fitted model can accurately reflect the curvature effect of topography on granular flow (Pudasaini and Hutter, 2003, 2007; Wang et al., 2004). The numerical model in this study encompasses these features and considers obstacles as a local deviation term, however, the global-type model by Juez et al. (2014) considers these features roughly into a reduced gravity without the feature of earth pressure effects and resistance-like source terms. As could be found in Fig. 6, the global-type model produces more errors compared with the bed-fitted model for deposition around obstacles. Therefore, a bed-fitted system with stress anisotropy (Pudasaini and Kroener, 2008) is a more suitable model in simulating dynamics and deposits around obstacles of rapid granular flow on steep terrain compared with the global system (Juez et al., 2014; Yuan et al., 2018; Castro-Orgaz et al., 2015).
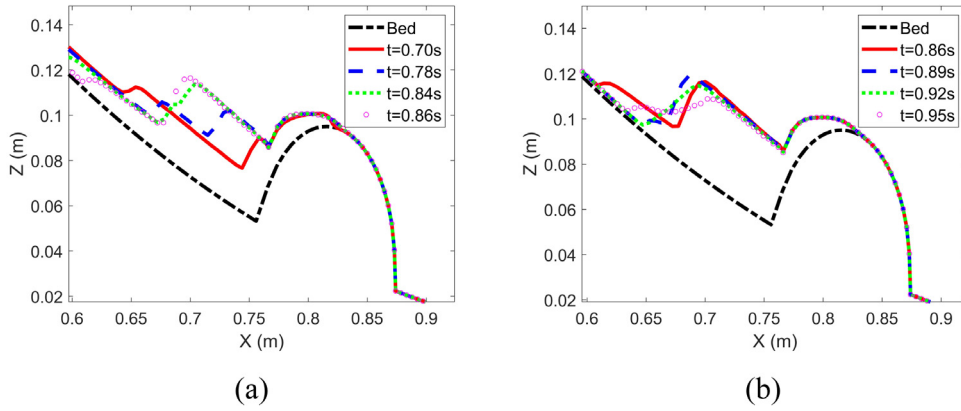
Fig. 7. Moving shock and rapid transition zone (a), relaxation of a shock to a deposit (b) in the center slice surface of granular flow facing a hemispherical obstacle.
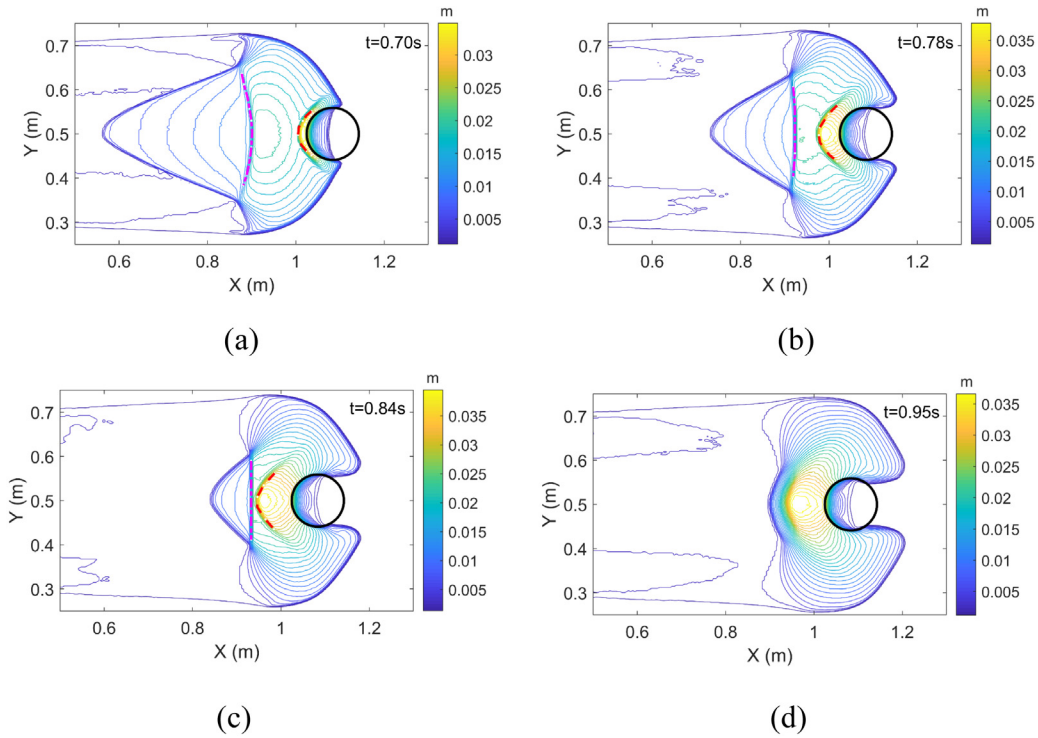

Fig. 8. Top view of a depth contour of granular flow facing a hemispherical obstacle. The red dashed line depicts shock and purple dash-dot line denotes rapid transition zone at different times.

4.1.3. Wave formation and interaction

The interaction of granular flow with obstacles involves complex shock wave formation and interaction, which play a key role in how granular flow evolves and deposits. Fig. 7 shows how the shock in front of the obstacle forms and evolves to a deposit. In Fig. 7a ($t = 0.70$ s), a strong bow shock forms in front of the obstacle, and a tailing rapid transition zone (RTZ) forms owing to a slowdown of granular flow on the gentle slope. The downstream shock moves upstream and the upstream tailing RTZ moves down, and they finally merge into a strong shock at $t = 0.86$ s. The shock then gradually relaxes to deposit owing to the bed resistance, as shown in Fig. 7b after $t = 0.92$ s.

A top view in Fig. 8 clearly shows the distribution of RTZ (purple dash-dot line) and shock (red dashed line). The tailing RTZ upstream is slightly curved, and the shock downstream is obviously curved. The RTZ moves downstream and the shock moves upstream. The two moving structures merge into a new shock when contacting, which later relaxes into a deposit owing to bed friction in Fig. 8d.
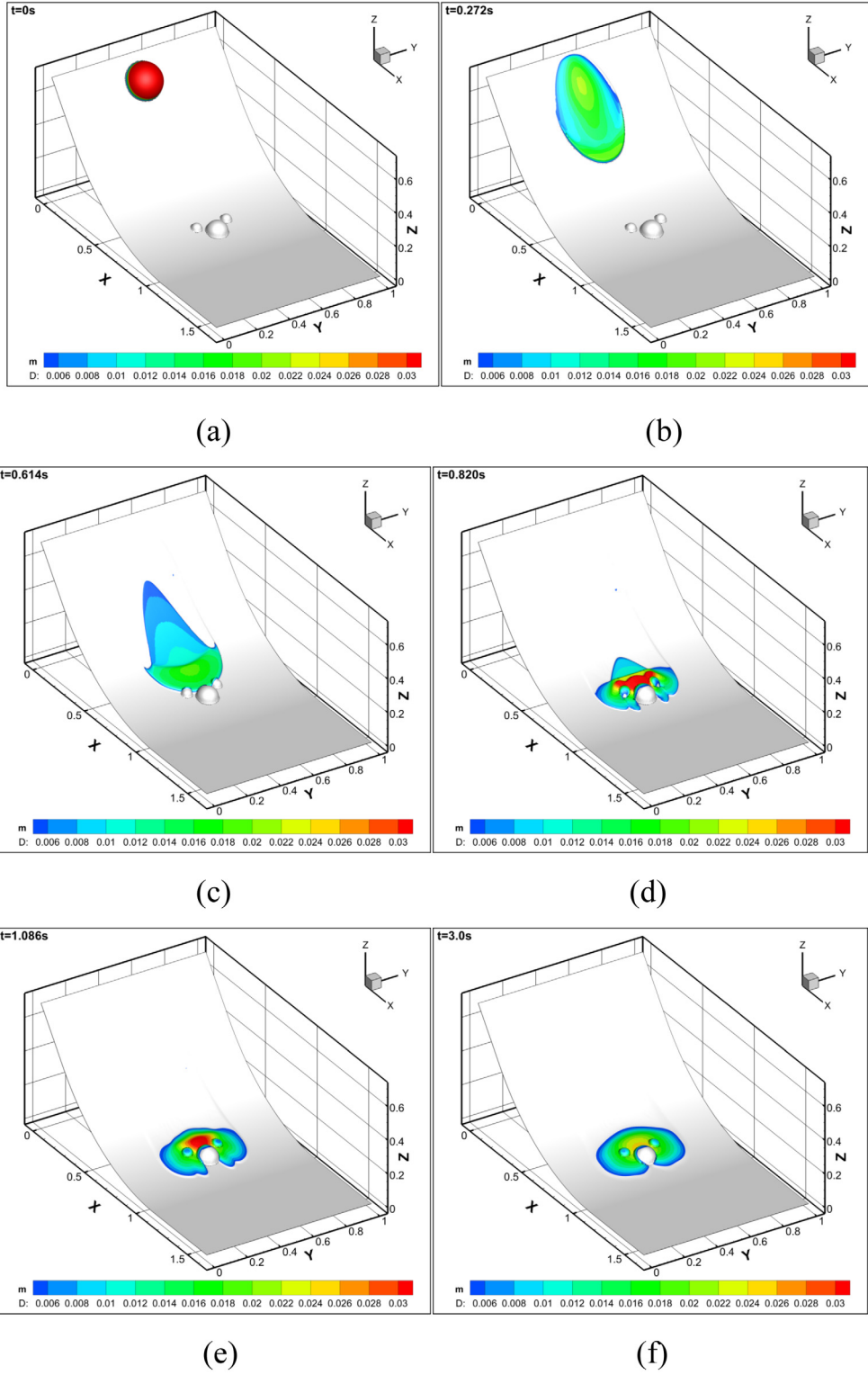
Fig. 9. Depth distribution evolution of granular flow past an obstacle of three hemi-spheres at different times.
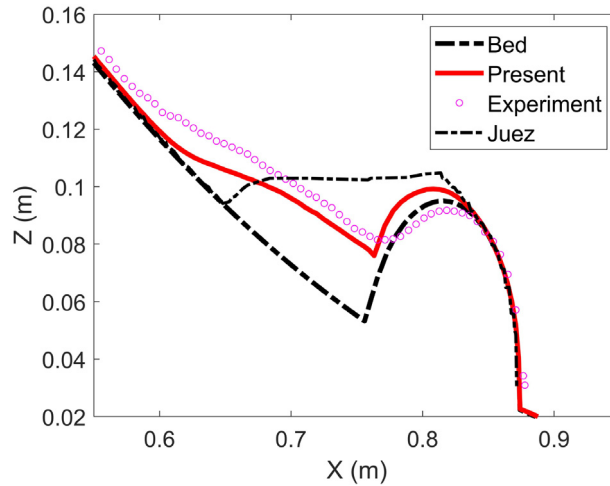
Fig. 10. Numerical results compared with Juez's experimental and computational results along the center slice for granular flow past three hemispherical obstacles.

4.2. Granular flow facing three hemispheres

4.2.1. Simulation setup

A system of multiple obstacles instead of a large obstacle is an alternate way to dissipate energy and change direction of granular flow for mitigation (Johannesson et al., 2009). Multiple obstacle systems have recently been applied by Kattel et al. (2018) and Kafle et al. (2019) to simulate the interactions between the particle–fluid mixture mass flows (Pudasaini, 2012) with obstacles and the complex dynamics. Therefore, we consider rapid granular flow facing an obstacle system of three hemispheres on a slope, as shown in Fig. 9a. The bed information is the same as that in 4.1. Two small hemispheres with radii of 29 mm were set in front of a large hemispherical obstacle. The positions of these obstacles were (1.0834, 0.5), (1.0248, 0.41), and (1.0248, 0.59) m, respectively. The initial granular material was a hemispherical bump set at (0.1624, 0.5) m with radius of 104 mm. A numerical model with a mesh of 400×400 and physical parameters of $\phi = \delta = 34°$ was constructed to simulate the runout of granular flow past the three hemispheres.

4.2.2. Dynamical behavior and granular deposition

Figs. 9a–9f show the full process previously described. The released granular material runs downward prior to contacting the obstacles. The front part first meets the two smaller obstacles. The run-up and bypass of the two smaller obstacles are shown in Figs. 9c and 9d. The main flow then enhances the depth in front of the large obstacle. There were three detached shocks in front of the obstacle system with different strengths that interact with one another, resulting in a trailing wavy shock structure, as shown in Fig. 9d. The wavy shock structure then interacted with the incoming flow and relaxed to a full deposit toward the obstacle system, as shown in Figs. 9e and 9f. Broadly speaking, similar shock structures and their interactions have been obtained for two-phase mass flows (Pudasaini, 2012) interacting with obstacles of different dimensions and constellations by Kattel et al. (2018) and Kafle et al. (2019).

Fig. 10 shows the deposit profile in the center slice surface alongside simulation results by Juez et al. (2014) and experimental results by Caviedes-Voullième et al. (2014). The present numerical model is in better agreement with the experimental data with regards to the tailing distribution and run-up results compared to model of Juez et al. (2014) in a global coordinate system. However, there are still some deviations from the experimental results.

4.2.3. Wave formation and interaction

Fig. 11 shows the shock wave formation, interaction, and relaxation for granular flow facing three hemispherical obstacles. Some features are similar with those in the case of a single hemispherical obstacle; however, the detailed spatial progression is slightly different, as shown in Fig. 12. At $t = 0.70$ s, three shocks (red dashed line) of different intensities form in front of each obstacle, almost independent of each other. The center shock is stronger than the other two shocks. Interactions between the three shocks as they move upstream produce a wavy shock at $t = 0.78$ s. The wavy shock moves upstream and merges with the upstream tailing RTZ (purple dash dot line) to form a new wavy shock at $t = 0.85$ s. The wavy shock then relaxes to form a complex deposit, as shown in Figs. 12d. These findings provide new insights into the complex behavior of granular flow facing an obstacle system, which has not yet been found in the straight slope case (Pudasaini and Kroener, 2008).
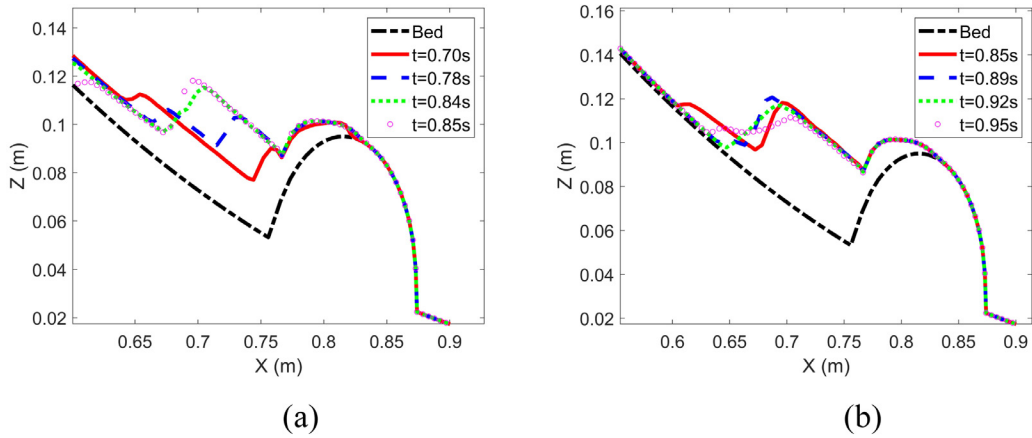
Fig. 11. Moving shock and rapid transition zone (a), relaxation of shock to the deposit (b) in the center slice surface for granular flow facing three hemispherical obstacles.
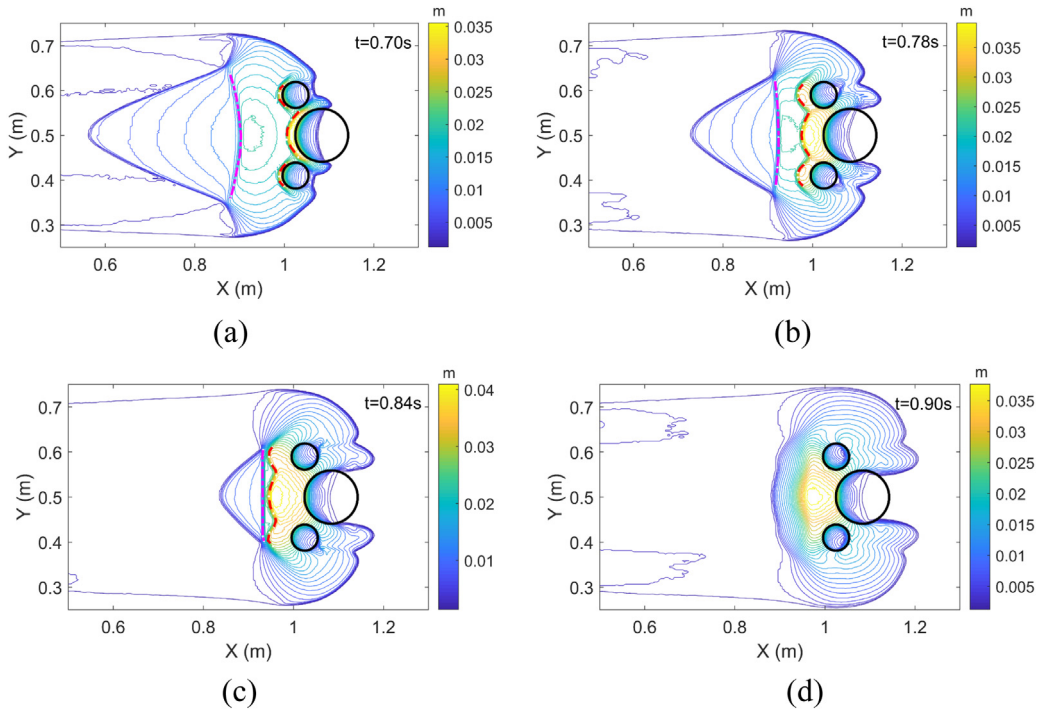

Fig. 12. Top view of a depth contour of granular flow facing three hemispherical obstacles. The red dashed line depicts the shock and the purple dash-dot line denotes rapid transition zone at different times.

5. Conclusions

We developed a numerical solver to compute fast granular flow facing obstacles on steep terrain. Several cases were simulated to verify the numerical model and the waves and deposit behavior of granular flow facing different obstacles were studied. The following includes a summary of conclusions along with some future perspectives.

(1) A depth-averaged model on bed-fitted terrain with obstacles treated as local bed deviation is selected to model granular flow facing obstacles on steep terrain. The model makes a compromise between the treatment of steep terrain and obstacle problem, which is able to describe both the run-up and bypass behavior of granular flow facing obstacles in a unified framework. A robust Riemann-free solver with a robust wetting–drying technique is established and verified by successful simulations of several fast granular flow cases, such as aluminum bar collapse, runout of granular flow on a slope, and granular flow past obstacles.

(2) There are multiple shock and flow structures in granular flow facing obstacles. Both run-up and bypass exist around the obstacles. Granular flow facing a single obstacle produces a detached shock moving upstream and an upstream tailing rapid transition zone that moves down. The shock merges with the rapid transition zone to form a new shock, which later relaxes to deposition.

(3) Fast granular flow facing an obstacle system of three hemispheres produces an upstream tailing rapid transition zone moving downstream and a downstream wavy shock resulting from the interaction of the three bow shocks in front of each obstacle. The downstream wavy shock moves upstream and merges with the upstream rapid transition zone to form a new curved shock, which later relaxes to a deposit owing to bed friction.

Considerable work remains to be studied in the field of interaction between granular flow and structure. The complex wave structure and its interaction requires physical interpretation. An accurate estimation of the impact force will be important for structural design in mountainous areas. An approach to designing an obstacle system for mitigating hazards related to granular flow will be valuable for geological applications.

CRediT authorship contribution statement

Su Yang: Investigation, Data curation, Software, Visualization, Writing - review & editing. **Xiaoliang Wang:** Supervision, Conceptualization, Methodology, Software, Investigation, Writing - original draft. **Qingquan Liu:** Conceptualization, Funding acquisition. **Menghan Pan:** Data curation, Visualization.

Declaration of competing interest

The authors declare that they have no known competing financial interests or personal relationships that could have appeared to influence the work reported in this paper.

Acknowledgments

References

An, Y., Wu, Q., Shi, C.Q., Liu, Q.Q., 2016. Three-dimensional smoothed-particle hydrodynamics simulation of deformation characteristics in slope failure. Géotechnique 66 (8), 670–680. http://dx.doi.org/10.1680/jgeot.15.p.222.

Anderson, J.D., 1990. Modern Compressible Flow. McGraw-Hill, Singapore.

Armanini, A., Rossi, G., Larcher, M., 2020. Dynamic impact of a water and sediments surge against a rigid wall. J. Hydraul. Res. 58 (2), 1–12. http://dx.doi.org/10.1080/00221686.2019.1579113.

Bi, Y.Z., Du, Y.J., He, S.M., Sun, X.P., Wang, D.P., Li, X.P., Liang, H., Wu, Y., 2018. Numerical analysis of effect of baffle configuration on impact force exerted from rock avalanches. Landslides 15 (5), 1029–1043. http://dx.doi.org/10.1007/s10346-018-0979-z.

Bui, H.H., Fukagawa, R., Sako, K., Ohno, S., 2008. Lagrangian meshfree particles method (SPH) for large deformation and failure flows of geomaterial using elastic–plastic soil constitutive model. Int. J. Numer. Anal. Methods Geomech. 32, 1537–1570. http://dx.doi.org/10.1002/nag.688.

Calvetti, F., Di, C.G., Vairaktaris, E., 2017. DEM assessment of impact forces of dry granular masses on rigid barriers. Acta Geotech. 12 (1), 129–144. http://dx.doi.org/10.1007/s11440-016-0434-z.

Castro-Orgaz, O., Hutter, K., Giraldez, J.V., Hager, W.H., 2015. Nonhydrostatic granular flow over 3-D terrain: New Boussinesq-type gravity waves? J. Geophys. Res. Earth Surf. 120 (1), 1–28. http://dx.doi.org/10.1002/2014jf003279.

Caviedes-Voullième, D., Juez, C., Murillo, J., García-Navarro, P., 2014. 2D dry granular free-surface flow over complex topography with obstacles. Part I:experimental study using a consumer-grade RGB-D sensor. Comput. Geosci. 73, 177–197. http://dx.doi.org/10.1016/j.cageo.2014.09.009.

Choi, C.E., Ng, C.W.W., Song, D., Kwan, J.S.H., Shiu, H.Y.K., Ho, K.K.S., Koo, R.C.H., 2014. Flume investigation of landslide debris–resisting baffles. Can. Geotech. J. 51 (5), 540–553. http://dx.doi.org/10.1139/cgj-2013-0115.

Cui, X., Gray, J.M.N.T., 2013. Gravity-driven granular free-surface flow around a circular cylinder. J. Fluid Mech. 720, 314–337. http://dx.doi.org/10.1017/jfm.2013.42.

Dai, Z., Huang, Y., Cheng, H., Xu, Q., 2016. SPH model for fluid–structure interaction and its application to debris flow impact estimation. Landslides 14 (3), 917–928. http://dx.doi.org/10.1007/s10346-016-0777-4.

Domnik, B., Pudasaini, S.P., 2012. Full two-dimensional rapid chute flows of simple viscoplastic granular materials with a pressure-dependent dynamic slip-velocity and their numerical simulations. J. Non-Newtonian Fluid Mech. 173, 72–86. http://dx.doi.org/10.1016/j.jnnfm.2012.03.001.

Domnik, B., Pudasaini, S.P., Katzenbach, R., Miller, S.A., 2013. Coupling of full two-dimensional and depth-averaged models for granular flows. J. Non-Newton. Fluid Mech. 201, 56–68. http://dx.doi.org/10.1016/j.jnnfm.2013.07.005.

Faug, T., 2015. Depth-averaged analytic solutions for free-surface granular flows impacting rigid walls down inclines. Phys. Rev. E 92 (6), 062310. http://dx.doi.org/10.1103/PhysRevE.92.062310.

Gray, J.M.N.T., Tai, Y.C., Noelle, S., 2003. Shock waves, dead zones and particle-free regions in rapid granular free-surface flows. J. Fluid Mech. 491, 161–181. http://dx.doi.org/10.1017/s0022112003005317.

Gray, J.M.N.T., Wieland, M., Hutter, K., 1999. Free surface flow of cohesionless granular avalanches over complex basal topography. Proc. R. Soc. Lond. Ser. A Math. Phys. Eng. Sci. 455, 1841–1874. http://dx.doi.org/10.1098/rspa.1999.0383.

Intrieri, E., Raspini, F., Fumagalli, A., Lu, P., Conte, S.D., Farina, P., Allievi, J., Ferretti, A., Casagli, N., 2018. The maoxian landslide as seen from space: detecting precursors of failure with Sentinel-1 data. Landslides 15 (1), 123–133. http://dx.doi.org/10.1007/s10346-017-0915-7.

Johannesson, T., Gauer, P., Issler, D., Lied, K., 2009. The Design of Avalanche Protection Dams. European Commision, Luxembourg.

Juez, C., Caviedes-Voullième, D., Murillo, J., García-Navarro, P., 2014. 2D dry granular free-surface flow over complex topography with obstacles. Part II: Numerical predictions of fluid structures and benchmarking. Comput. Geosci. 73, 142–163. http://dx.doi.org/10.1016/j.cageo.2014.09.010.

Kafle, J., Kattel, P., Mergili, M., Fischer, J.T., Pudasaini, S.P., 2019. Dynamic response of submarine obstacles to two-phase landslide and tsunami impact on reservoirs. Acta Mech. 230 (9), 3143–3169. http://dx.doi.org/10.1007/s00707-019-02457-0.

Kattel, P., Kafle, J., Fischer, J.T., Mergili, M., Tuladhar, B.M., Pudasaini, S.P., 2018. Interaction of two-phase debris flow with obstacles. Eng. Geol. 242, 197–217. http://dx.doi.org/10.1016/j.enggeo.2018.05.023.

Koch, T., Grave, R., Hutter, K., 1994. Unconfined flow of granular avalanches along a partly curved surface. Proc. R. Soc. A 445, 399–413. http://dx.doi.org/10.1016/0148-9062(94)90382-4.

Kurganov, A., Petrova, G., 2007. A second-order well-balanced positivity preserving central-upwind scheme for the saint-venant system. Commun. Math. Sci. 5 (1), 133–160. http://dx.doi.org/10.4310/cms.2007.v5.n1.a6.

LeVeque, R.J., 2002. Finite Volume Methods for Hyperbolic Problems. Cambridge University Press, Cambridge.

Liang, Q.H., Marche, F., 2009. Numerical resolution of well-balanced shallow water equations with complex source terms. Adv. Water Resour. 32 (6), 873–884. http://dx.doi.org/10.1016/j.advwatres.2009.02.010.

Mergili, M., Jaboyedoff, M., Pullarello, J., Pudasaini, S.P., 2020a. Back calculation of the 2017 Piz Cengalo–Bondo landslide cascade with r.avaflow: what we can do and what we can learn. Nat. Hazards Earth Syst. Sci. 20, 505–520. http://dx.doi.org/10.5194/nhess-20-505-2020.

Mergili, M., Pudasaini, S.P., Emmer, A., Fischer, J.T., Cochachin, A., Frey, H., 2020b. Reconstruction of the 1941 GLOF process chain at Lake Palcacocha (Cordillera Blanca, Peru). Hydrol. Earth Syst. Sci. 24, 93–114. http://dx.doi.org/10.5194/hess-24-93-2020.

Pudasaini, S.P., 2012. A general two-phase debris flow model. J. Geophys. Res 117, F03010. http://dx.doi.org/10.1029/2011jf002186.

Pudasaini, S.P., 2014. Dynamics of submarine debris flow and tsunami. Acta Mech. 225 (8), 2423–2434. http://dx.doi.org/10.1007/s00707-014-1126-0.

Pudasaini, S.P., Hutter, K., 2003. Rapid flow of dry granular masses down curved and twisted channels. J. Fluid Mech. 495, 193–208. http://dx.doi.org/10.1017/s0022112003006141.

Pudasaini, S.P., Hutter, K., 2007. Avalanche Dynamics: Dynamics of Rapid Flows of Dense Granular Avalanches. Springer, Berlin.

Pudasaini, S.P., Hutter, K., Hsiau, S.S., Tai, S.C., Wang, Y., Katzenbach, R., 2007. Rapid flow of dry granular materials down inclined chutes impinging on rigid walls. Phys. Fluids 19, 053302. http://dx.doi.org/10.1063/1.2726885.

Pudasaini, S.P., Kroener, C., 2008. Shock waves in rapid flows of dense granular materials: theoretical predictions and experimental results. Phys. Rev. E 78, 041308. http://dx.doi.org/10.1103/PhysRevE.78.041308.

Pudasaini, S.P., Mergili, M., 2019. A multi-phase mass flow model. J. Geophys. Res. Earth Surf. 124, 2920–2942. http://dx.doi.org/10.1029/2019JF005204.

Savage, S.B., Hutter, K., 1989. The motion of a finite mass of granular material down a rough incline. J. Fluid Mech. 199 (1), 177–215. http://dx.doi.org/10.1017/s0022112089000340.

Tang, J., Hu, S., 2018. A debris-flow impact pressure model combining material characteristics and flow dynamic parameters. J. Mt. Sci. 15 (12), 2721–2729. http://dx.doi.org/10.1007/s11629-018-5114-z.

Tang, C., Rengers, N., Van Asch, T.W.J., Yang, Y.H., Wang, G.F., 2011. Triggering conditions and depositional characteristics of a disastrous debris flow event in Zhouqu city, Gansu Province, northwestern China. Nat. Hazards Earth Syst. Sci. 11 (11), 2903–2912. http://dx.doi.org/10.5194/nhess-11-2903-2011.

Teufelsbauer, H., Wang, Y., Pudasaini, S.P., Borja, R.I., Wu, W., 2011. DEM simulation of impact force exerted by granular flow on rigid structures. Acta Geotech. 6 (3), 119–133. http://dx.doi.org/10.1007/s11440-011-0140-9.

Wang, D., Chen, Z., He, S., Liu, Y., Tang, H., 2018. Measuring and estimating the impact pressure of debris flows on bridge piers based on large-scale laboratory experiments. Landslides 15 (7), 1331–1345. http://dx.doi.org/10.1007/s10346-018-0944-x.

Wang, Y., Hutter, K., Pudasaini, S.P., 2004. The Savage-Hutter theory: A system of partial differential equations for avalanche flows of snow, debris, and mud. Z. Angew. Math. Mech. 84 (8), 507–527. http://dx.doi.org/10.1002/zamm.200310123.

Wang, X.L., Li, J.C., 2017. A new solver for granular avalanche simulation: Indoor experiment verification and field scale case study. Sci. China Phys. Mech. Astron. 60 (12), 124712. http://dx.doi.org/10.1007/s11433-017-9093-y.

Yuan, L., Liu, W., Zhai, J., Wu, S.F., Patra, A.K., Pitman, E.B., 2018. Refinement on non-hydrostatic shallow granular flow model in a global Cartesian coordinate system. Comput. Geosci. 22 (1), 87–106. http://dx.doi.org/10.1007/s10596-017-9672-x.

Zhou, G.G.D., Du, J., Song, D., Choi, C.E., Hu, H.S., Jiang, C., 2020. Numerical study of granular debris flow run-up against slit dams by discrete element method. Landslides 17 (3), 585–595. http://dx.doi.org/10.1007/s10346-019-01287-4.